AIAA JOURNAL
Vol. 30, No. 4, April 1992

Linear Stability of Three-Dimensional Boundary Layers over Axisymmetric Bodies at Incidence

R. E. Spall* and M. R. Malik†
High Technology Corporation, Hampton, Virginia 23666

The linear stability of the fully three-dimensional boundary layer formed over a 6:1 prolate spheroid at 10-deg incidence is investigated using a modified version of the linear stability code COSAL. For this case, both Tollmien-Schlichting and crossflow disturbances are relevant in the transition process. The predicted location of the onset of transition using the e^N method compares favorably with experimental results of Meier and Kreplin. Using a value of $N = 10$, the predicted location is located approximately 10% upstream of the experimentally determined location. Results also indicate that the direction of disturbance propagation is dependent on the type of disturbance and, hence, the dimensional frequency. We also investigate characteristics of the most amplified disturbances at various streamwise locations.

I. Introduction

THE ability to predict the location of boundary-layer transition is of crucial importance in the application of laminar flow control (LFC) technology to both subsonic and supersonic aircraft design. Because much of the transition process in low-disturbance environments involves linear amplification, the onset of transition can be correlated using linear stability theory in conjunction with the e^N method, where the exponent N is given as

$$N = \ln(A/A_0) = \int_{S_0}^{S_t} \sigma(s)\, ds \tag{1}$$

where A_0 is the amplitude of the internalized disturbance at the onset of instability and σ is its amplification rate. The value of N is obtained through comparisons with experimental data for the onset of transition. The e^N method, first used by Smith and Gamberoni,[1] has been found to work for a wide class of flows, which include Tollmien-Schlicting (TS) waves, crossflow instability in three-dimensional flows, and Goertler instability along concave walls. It has been found (see, e.g., Ref. 2) that the same value (about 9–11) of the exponent N (herein referred to as N factor) can correlate low-disturbance transition data regardless of the primary instability mode. The e^N method provides a useful tool for correlating the onset of transition with control parameters such as pressure gradient, wall heat/mass transfer, wall curvature, etc.

The flowfield over an aerospace vehicle is, in general, fully three dimensional. However, due to the ease of accurate computation, all previous three-dimensional stability studies (with the exception of Ref. 3) have employed simple three-dimensional mean flows (e.g., rotating disk, infinite swept wing, or tapered swept wings with straight isobars). For example, the compressible linear stability code COSAL[4] utilizes the mean flow for a swept wing with the conical flow similarity transformation in the spanwise direction. This technique provides a quick way of analyzing the stability of three-dimensional mean flows in the midspan region of certain swept wings. However, for general wing configurations, particularly for supersonic flow, and for fuselages and nacelles, fully three-dimensional flowfields are required, and it is of interest to study such flows.

Received Dec. 17, 1990; revision received May 9, 1991; accepted for publication May 13, 1991.

*Research Assistant, 28 Research Drive. Member AIAA.
†President, 28 Research Drive. Member AIAA.

We have modified the COSAL code for application to fully three-dimensional flows, and in this paper, we use it to investigate the linear stability of the three-dimensional boundary-layer flow formed over a prolate spheroid at an angle of attack (see Fig. 1). The geometry and flow conditions are the same as in the experiment of Meier and Kreplin.[5] Comparisons are made between our computed location of the onset of transition (which in this case depends on the azimuthal angle) and the measurements of Meier and Kreplin. In addition, detailed results regarding the stability of this fully three-dimensional boundary layer are presented. The mean flow was computed by using a second-order-accurate finite difference procedure coded by Wie.[6] This procedure employs Matsuno's finite difference method[7] and is well suited for three-dimensional boundary-layer computations, including regions of reversed crossflow.

II. Numerical Procedure

The three-dimensional boundary-layer equations for the compressible laminar flow in a body-oriented coordinate system may be written as the following:

Continuity equation:

$$\frac{\partial}{\partial x}(\rho u h_2 \sin\varphi) + \frac{\partial}{\partial y}(\rho v h_1 \sin\varphi) + \frac{\partial}{\partial z}(\rho w h_1 h_2 \sin\varphi) = 0 \tag{2}$$

x-momentum equation:

$$\frac{\rho u}{h_1}\frac{\partial u}{\partial x} + \frac{\rho v}{h_2}\frac{\partial u}{\partial y} + \rho w \frac{\partial u}{\partial z} - \rho u^2 K_1 \cot\varphi + \rho v^2 K_2 \csc\varphi + \rho u v K_{12} = -\frac{\csc^2\varphi}{h_1}\frac{\partial p}{\partial x} + \frac{\cot\varphi \csc\varphi}{h_2}\frac{\partial p}{\partial y} + \frac{\partial}{\partial z}\left(\mu \frac{\partial u}{\partial z}\right) \tag{3}$$

y-momentum equation:

$$\frac{\rho u}{h_1}\frac{\partial v}{\partial x} + \frac{\rho v}{h_2}\frac{\partial v}{\partial y} + \rho w \frac{\partial v}{\partial z} - \rho v^2 K_2 \cot\varphi + \rho u^2 K_1 \csc\varphi + \rho u v K_{21} = \frac{\cot\varphi \csc\varphi}{h_1}\frac{\partial p}{\partial x} - \frac{\csc^2\varphi}{h_2}\frac{\partial p}{\partial y} + \frac{\partial}{\partial z}\left(\mu \frac{\partial v}{\partial z}\right) \tag{4}$$

Energy equation:

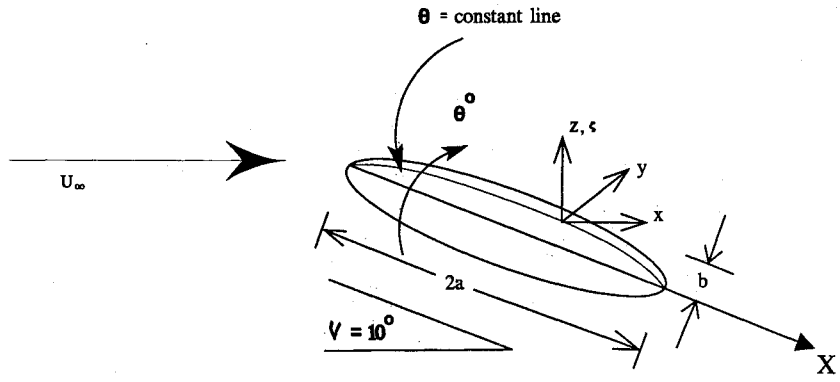

Fig. 1 Geometry and coordinate system for prolate spheroid.

$$\frac{\rho u}{h_1}\frac{\partial H}{\partial x} + \frac{\rho v}{h_2}\frac{\partial H}{\partial y} + \rho w \frac{\partial H}{\partial z} = \frac{\partial}{\partial z}\left\{\frac{\mu}{Pr}\frac{\partial H}{\partial z} + \mu\left(1 - \frac{1}{Pr}\right)\frac{\partial}{\partial z}\left(\frac{V^2}{2}\right)\right\} \tag{5}$$

In Eqs. (2–5), (u, v, w) are the velocity components in the (x, y, z) directions, V the total velocity given by $V = (u^2 + v^2 + 2uv\cos\varphi)^{1/2}$, H the total enthalpy, Pr the constant Prandtl number, and μ the dynamic viscosity. The perfect gas equation and Sutherland's viscosity law are used to close the equation set. The parameters K_1, K_2, K_{12}, and K_{21} appearing in the momentum equations are given as

$$K_1 = \frac{1}{h_1 h_2 \sin\varphi}\left\{\frac{\partial}{\partial x}(h_2\cos\varphi) - \frac{\partial h_1}{\partial y}\right\} \tag{6}$$

$$K_2 = \frac{1}{h_1 h_2 \sin\varphi}\left\{\frac{\partial}{\partial y}(h_1\cos\varphi) - \frac{\partial h_2}{\partial x}\right\} \tag{7}$$

$$K_{12} = \frac{1}{h_1 h_2 \sin^2\varphi}\left\{(1 + \cos^2\varphi)\frac{\partial h_1}{\partial y} - 2\cos\varphi\frac{\partial h_2}{\partial x}\right\} \tag{8}$$

$$K_{21} = \frac{1}{h_1 h_2 \sin^2\varphi}\left\{(1 + \cos^2\varphi)\frac{\partial h_2}{\partial x} - 2\cos\varphi\frac{\partial h_1}{\partial y}\right\} \tag{9}$$

The variable φ represents the angle between the x and y surface coordinates, and if the grid is orthogonal, as in the present calculations, $\varphi = 90$ deg.

The boundary layer was computed using analytic metric coefficients and edge velocity boundary conditions. The metric coefficients h_1 and h_2 are given as[8]

$$h_1 = \left\{\frac{1 + \xi^2(t^2 - 1)}{1 - \xi^2}\right\}^{1/2} \tag{10}$$

$$h_2 = t\sqrt{1 - \xi^2} \tag{11}$$

where $\xi = (X/a) - 1$ and $t = b/a$ (see Fig. 1).

The inviscid velocity components are given by[9]

$$u_e/U_\infty = V_0(t)\cos\upsilon\cos\tau - V_{90}(t)\sin\upsilon\sin\tau\cos\theta \tag{12}$$

$$v_e/U_\infty = V_{90}(t)\sin\upsilon\sin\theta \tag{13}$$

Here, υ is the angle of attack, θ the azimuthal angle, and τ the angle between the line tangent to the ellipse and the positive X axis and is given by

$$\cos\tau = \frac{\sqrt{1 - \xi^2}}{[1 + \xi^2(t^2 - 1)]^{1/2}} \tag{14}$$

where $\tau < 0$ if $\xi > 1$ and $\tau > 0$ if $\xi < 1$.

$V_0(t)$ and $V_{90}(t)$ are functions of the aspect ratio of the ellipse and are given as

$$V_0(t) = \frac{(1 - t^2)^{3/2}}{(1 - t^2)^{1/2} - \frac{1}{2}t^2\ln\left[\frac{1 + (1 - t^2)^{1/2}}{1 - (1 - t^2)^{1/2}}\right]} \tag{15}$$

$$V_{90}(t) = \frac{2V_0(t)}{2V_0(t) - 1} \tag{16}$$

A Levy-Lees-type transformation is used in order to remove the singularity at $X = 0$. This transformation is of the form

$$x = x, \qquad y = y, \qquad \zeta = \sqrt{\frac{\rho_e u_e}{\mu_e s}}\int_0^z \frac{\rho}{\rho_e}\,dz \tag{17}$$

Matsuno's finite difference method is used to advance the solution in the streamwise direction (see Refs. 6 and 7). The scheme is half-implicit in the ζ (the transformed wall-normal coordinate) direction, explicit in the y direction, noniterative, and second-order accurate. One advantage of Matsuno's scheme is that the y derivatives are formed independent of the direction of the sign of the crossflow velocity. Other schemes commonly require modification in regions of reversed crossflow (due to the elliptic nature of the flow). A modified version of Matsuno's scheme is used where the solution is not available over the entire finite difference molecule, such as occurs at the side (y-direction) boundary or where flow separation occurs off the plane of symmetry. Under these circumstances, a three-point backward difference is used in the y direction (see Ref. 6).

The stability results presented in the present paper have been obtained using a modified version of the linear stability code COSAL. The modifications include provisions to accept fully three-dimensional boundary-layer profiles. In COSAL, a parallel flow approximation is employed, and thus the disturbed flow (say the u component) may be represented as

$$u(x, y, z, t) = U(z) + \varepsilon\hat{u}(z)e^{i(\alpha x + \beta y - \omega t)} \tag{18}$$

where α and β are the disturbance wave numbers in the x and y directions, respectively, and ω is the disturbance frequency. The compressible, linear (small ε) stability equations can be represented as

$$\left(A\frac{d^2}{dz^2} + B\frac{d}{dz} + C\right)\bar{\Phi} = 0 \tag{19}$$

where $\bar{\Phi}$ is a five-element vector defined as $[\alpha\hat{u} + \beta\hat{v}, \hat{w}, \hat{p}, \hat{T}, \alpha\hat{v} - \beta\hat{u}]$.

The elements of the A, B, and C matrices are given in Malik and Orszag.[10] This system is solved subject to the boundary conditions:

$$\Phi_1 = \Phi_2 = \Phi_4 = \Phi_5 = 0 \quad \text{at} \quad z = 0 \tag{20a}$$

$$\Phi_1, \Phi_2, \Phi_4, \Phi_5 \to 0 \quad \text{as} \quad z \to \infty \tag{20b}$$

This system provides, given the Reynolds number R, a complex dispersion relation of the form:

$$\omega = \omega(\alpha, \beta) \tag{21}$$

For the temporal theory that is used in COSAL, α and β are real and ω is complex. The temporal theory results in a linear eigenvalue problem for ω, allowing a direct analysis using generalized eigenvalue techniques. The stability equations are discretized using a second-order-accurate finite difference formulation on a staggered grid. The staggered grid eliminates the need for pressure boundary conditions.

For the temporal problem, the dispersion relation contains four arbitrary parameters, namely, α, β, ω_r, and ω_i. For N-factor calculations, one follows a disturbance of fixed physical frequency f, which sets one condition. Two more conditions are provided by the complex dispersion relation, Eq. (21). The additional condition needed to remove the arbitrariness in the problem is the requirement that the growth rate ω_i be maximized with respect to α and β. Thus, the wave numbers α and β are uniquely determined as a result of this procedure. The wave orientation ψ is measured with respect to the freestream inviscid flow direction and can then be defined as

$$\psi = \tan^{-1}(\beta/\alpha) \tag{22}$$

for a given location on the body (see Fig. 2).

For a disturbance of fixed frequency ω_r, whose temporal growth rate is a maximum, we can write

$$d\omega_r = \frac{\partial \omega_r}{\partial \alpha} d\alpha + \frac{\partial \omega_r}{\partial \beta} d\beta = 0 \tag{23}$$

$$d\omega_i = \frac{\partial \omega_i}{\partial \alpha} d\alpha + \frac{\partial \omega_i}{\partial \beta} d\beta = 0 \tag{24}$$

From Eqs. (23) and (24), it follows that

$$\frac{\partial \omega_r}{\partial \beta} \Big/ \frac{\partial \omega_r}{\partial \alpha} = \frac{\partial \omega_i}{\partial \beta} \Big/ \frac{\partial \omega_i}{\partial \alpha} \tag{25}$$

which is also the condition for the group velocity ratio ($\omega_\beta/\omega_\alpha$) to be real. The group velocity angle

$$\hat{\psi} = \tan^{-1}(\omega_\beta/\omega_\alpha) \tag{26}$$

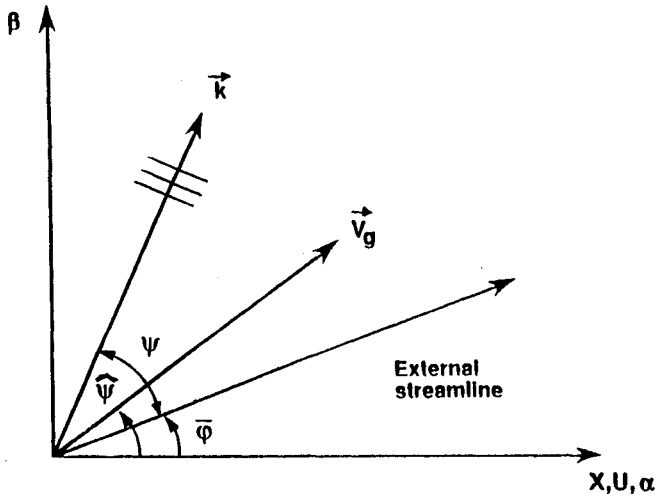

Fig. 2 Coordinate convention used in COSAL: k and V_g represent the wave number and group velocity vectors, respectively.

provides the direction in which the integration in Eq. (1) is carried out.

To perform the integration, the temporal amplification rate ω_i needs to be converted to a spatial rate, which is accomplished by using the group velocity transformation[11]

$$\sigma = \frac{\omega_i}{|\mathrm{Re}(V_g)|} \tag{27}$$

where $V_g = (\omega_\alpha, \omega_\beta)$ is the complex group velocity.

The disturbance amplitude A at some downstream location is given as $A = A_0 e^N$, where A_0 is the amplitude of some disturbance at the critical point s_0. The onset of transition is assumed to occur when N reaches some predetermined value, typically in the range of 9–11.

As mentioned previously, the amplitude ratio is computed by following a disturbance of fixed-dimensional frequency in the direction determined by the group velocity ratio. Because this direction is unknown at the time of the boundary-layer calculation, the boundary-layer profiles must be interpolated between grid points as a given disturbance is followed downstream. This interpolation is performed on the boundary-layer computational grid. The metric coefficients h_1 and h_2 provide the relationship between this domain and the physical domain utilized in the stability calculations. We also note that, due to practical limits on computer resources, the boundary-layer profiles are read into the stability code at selected locations only. For the case of the prolate spheroid, all points in the circumferential direction were included, whereas 66 points were included in the streamwide direction.

III. Results and Discussion

In this section, we discuss results for the low Mach number ($M = 0.132$) flow over an ellipsoid of revolution of fineness ratio 6:1 at an angle of attack $v = 10$ deg. The length of the ellipsoid is taken as $2a = 7.874$ ft. This same configuration is discussed in the experimental work of Meier and Kreplin[5] and the numerical work of Cebeci and Chen[3]. We chose the Reynolds number $Re = 6.6 \times 10^6$ based on private communication with Kreplin (although the Reynolds number in Ref. 5 is given as 7.2×10^6). The results are presented using a normalized axial coordinate ξ, such that $-1 \le \xi \le 1$ corresponds to $0 \le X \le 2a$, and the angle θ, for which $\theta = 0$ deg on the windward symmetry line and $\theta = 180$ deg on the leeward symmetry line. The geometry and coordinate system are shown in Fig. 1.

The analytic inviscid velocity distribution and metric coefficients were used in the solution of the boundary-layer equations (see Sec. II). Figure 3 presents a contour plot of the distribution of C_p over the ellipsoid. Note that an adverse pressure gradient is encountered at approximately $\xi = -0.9$ on the leeward symmetry line and $\xi = 0.9$ on the windward symmetry line. This immediately suggests that transition on the leeward symmetry line will take place much sooner than transition on the windward symmetry line since boundary layers usually become highly unstable in regions of adverse pressure gradient.

The boundary-layer equations were initially solved using 300 grid points in the streamwise direction, with clustering toward

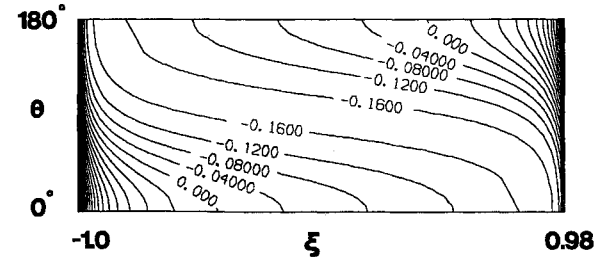

Fig. 3 Contour plot of constant C_p on a 6:1 prolate spheroid at $M = 0.132$, $V = 10$ deg, and $Re = 6.6 \times 10^6$.

the nose region. In the circumferential direction, 31 points were used, resulting in a constant $\Delta\theta$ of 6 deg. The points were distributed in a manner such that the domain of dependence requirement was not violated (see Ref. 6). In addition, a constant $\Delta\zeta$ spacing of 0.1 was used in the wall normal direction. We note that in the work of Cebeci and Chen[3] oscillations in the wall shear stress were found starting at $\xi = -0.476$ and near $\theta = 131$ deg, and that these increased with increasing ξ (toward an initial separation point at $\xi = -0.463$). Using a refined grid, Cebeci and Chen determined the initial separation point to be at $\xi = -0.4759$ and $\theta = 132.5$ deg. This compares to the approximate separation point $\xi = -0.46$ and $\theta = 132$ deg determined in the present study using the aforementioned grid distribution. Since we do not compute the boundary layer for values of $\theta > \theta_{sep}$ (ξ) as ξ increases, we do not known if the problem with the oscillations in wall shear stress would be encountered with Matsuno's scheme. To assess the sensitivity of the boundary layer to grid refinement, we made additional calculations of the boundary layer using 600 points in the streamwise direction and 61 points in the circumferential direction. Essentially no change was found in the boundary-layer profiles or the location of separation. The boundary-layer solution obtained using the 600 × 61 grid was used in the stability calculations that follow.

The boundary-layer computational domain is depicted in Fig. 4, which also shows contours of constant crossflow Reynolds number, defined as

$$Re_{cf} = \frac{U_n \delta_{0.1}}{\nu}$$

where U_n is the maximum velocity in the crossflow direction and $\delta_{0.1}$ is the distance from the wall at which the crossflow velocity decreases to 0.1 U_n. The cross-hatched area has been excluded from the domain of the boundary-layer calculation (due to separation). Also marked in the figure is the location of the initial separation point. Since transition takes place upstream of this point, the exclusion of the region downstream is of no consequence here. The plot indicates a rapid increase in crossflow Reynolds number as the separation point is approached. This results from an increase in the crossflow length scale as the region of adverse pressure gradient is encountered near the leeward line of symmetry. Note the occurrence of a local minimum in the crossflow Reynolds number just upstream of the initial separation point.

Figure 5 shows computed crossflow velocity profiles at locations $\theta = 80$, 120, 130, 140, 150, and 160 deg and $\xi = -0.68$. Profiles at several of these locations presented in Cebeci and Chen[3] compare favorably with our results. Note that a reversal occurs in the crossflow velocity profiles as θ increases beyond about 130 deg, which we later show to have important consequences in terms of the flow stability. The crossflow reversal is a result of the change in the pressure gradient from favorable to adverse as θ is increased for a fixed ξ, which can be seen by examining Fig. 3.

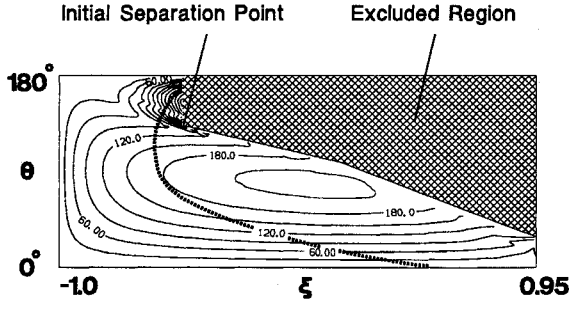

Fig. 4 Contour plot of constant crossflow Reynolds number: short-dashed line represents location of transition predicted using COSAL with $N = 10$.

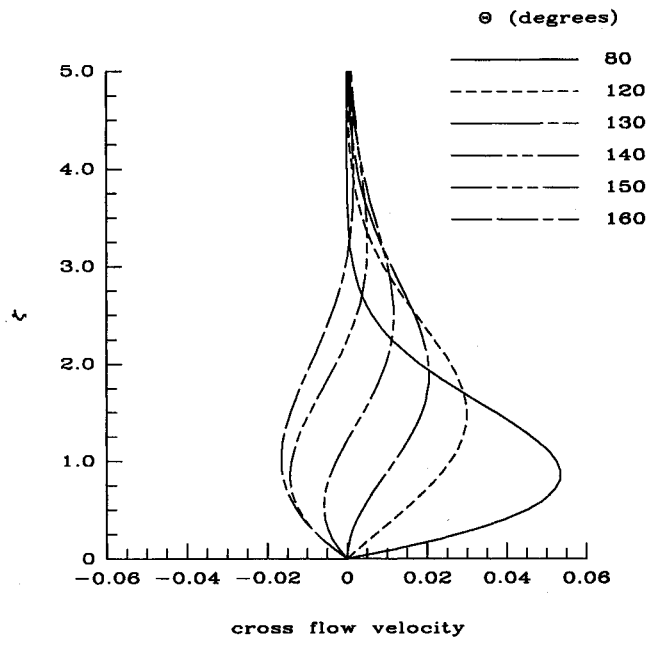

Fig. 5 Crossflow velocity profiles at $\xi = -0.68$ for various values of θ.

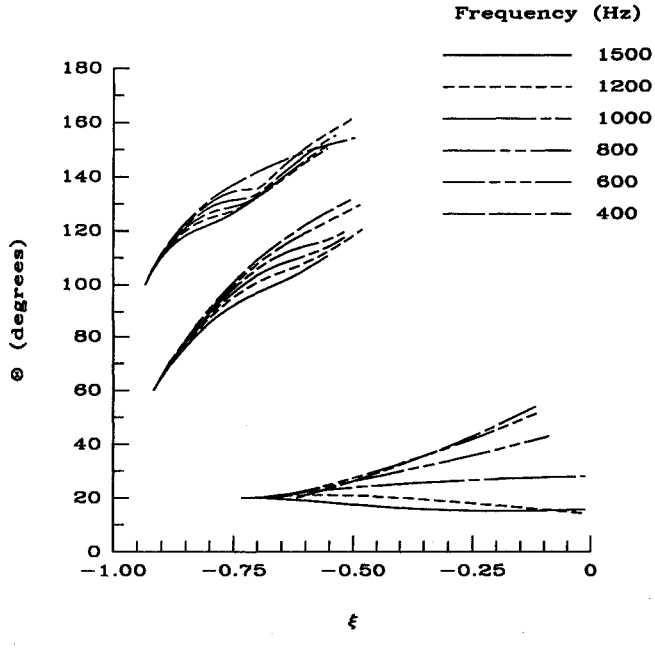

Fig. 6 Trajectory paths for disturbances originating near critical points.

After establishing the accuracy of the boundary-layer solution, we proceed to investigate the stability characteristics of the flow. We investigate the stability of a series of disturbances (f = 400, 600, 800, 1000, 1200, and 1500 Hz) originating near the critical points at angles $\theta = 20$, 60, and 100 deg. First, the initial points (the value of ξ at which the disturbances begin to amplify) were determined. It was found that, for a fixed θ, these disturbances begin to amplify at nearly the same ξ, which is a consequence of the inviscid nature of the instability at these values of θ. The crossflow Reynolds numbers at the three initial points are near 50. The N-factor calculations are started at the critical points and carried along rays defined by Eq. (26). The trajectories of these disturbances, as determined from the group velocity ratio, are plotted in Fig. 6. The corresponding N-factor calculations are shown in Figs. 7a–7c. If we consider the onset of transition to occur at N =

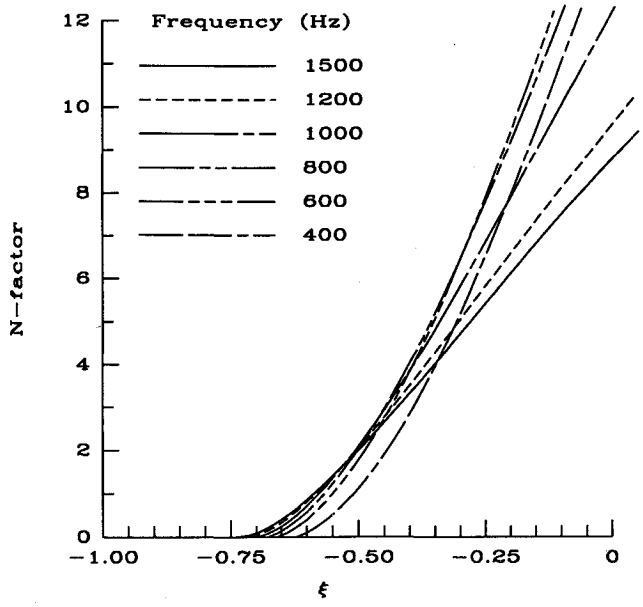

a) θ = 20 deg

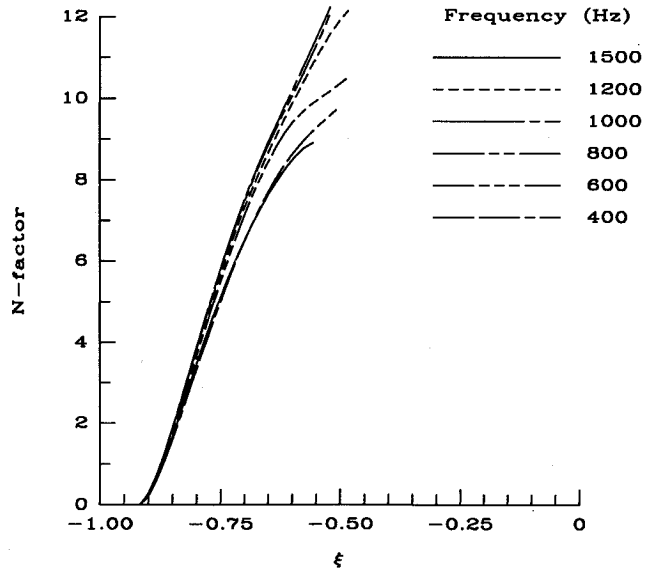

b) θ = 60 deg

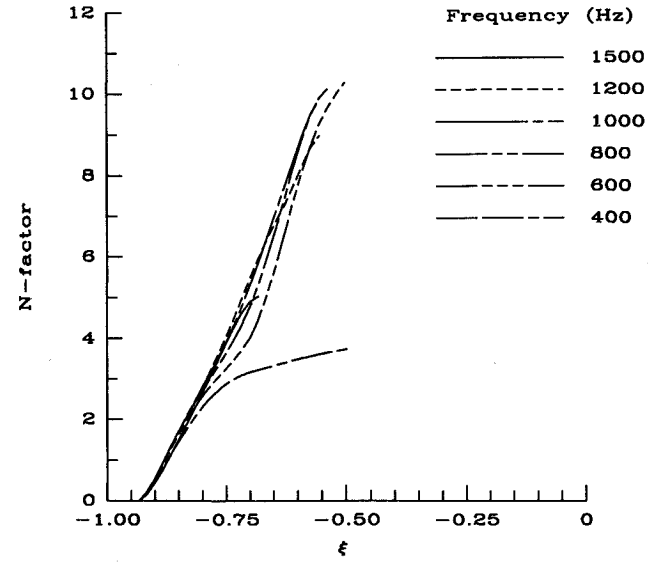

c) θ = 100 deg

Fig. 7 ***N*-factor calculations for disturbances originating at three different θ coordinates.**

10, then for the disturbances originating at θ = 20 deg, ξ_{tr} = −0.18; for θ = 60 deg, ξ_{tr} = −0.61; and for θ = 100 deg, ξ_{tr} = −0.56. For θ = 20 deg, the frequencies f = 600 and 800 Hz result in transition at approximately the same axial location. The circumferential locations at transition for these frequencies range from 40 to 50 deg, as shown in Fig. 6. For higher frequencies, estimated transition locations are farther downstream and the disturbances follow paths of nearly constant θ. We later show that the lower frequency waves possess characteristics of crossflow disturbances and the higher frequencies possess TS-type disturbances. For disturbances originating at θ = 60 and 100 deg, the highest amplitude ratios result from frequencies between 800–1200 and 600–1000 Hz, respectively. We note that the different frequency disturbances travel along an increasingly common path as the azimuthal angle for the initial disturbance is increased. On a practical note, this behavior simplifies the task of predicting the transition front using the *N*-factor method. Also indicated in Fig. 6 is the tendency of the higher frequencies originating at θ = 100 deg to follow paths of nearly constant θ for $-0.75 \leq \xi \leq -0.7$. An abrupt change in path then takes place for $\xi > -0.7$. This is shown later to be due to the changing orientation of the wave front with respect to the freestream potential flow.

The present normal mode analysis is performed to compute the most amplified disturbance at discrete streamwise locations. Such an analysis can only reveal the local stability characteristics of the given boundary-layer profiles. Actual evolution of a fixed-frequency disturbance in a three-dimensional boundary layer is more complicated and would require an analysis of the type used in Balakumar and Malik.[12] The abrupt change in disturbance path noted earlier may be smeared out in such an analysis. In any case, it is important to note that in the present paper we are only following the most amplified fixed-frequency mode at locations determined by the associated group velocity. What relevance, if any, this single normal mode calculation has on the evaluation of disturbances is not clear.

The strong dependency of the disturbance trajectories on frequency and on the initial disturbance location brings up another point. In some previous investigations of transonic flow over a swept wing, the integration path was satisfactorily approximated by following the inviscid flow velocity vector.[13] As shown in Fig. 6, this may not be an acceptable approximation for flow over fuselage-type bodies. Consider, for instance, the disturbances originating at θ = 20 deg. The frequency f = 400 Hz closely approximates the integration path as determined by the inviscid flow velocity vector, but as the frequency is increased, the disturbances track at progressively lower values of θ. Thus, for the higher frequencies, *N*-factor calculations are likely to give misleading results if the integration were performed in a direction determined by the external inviscid streamline.

To gain more insight into the stability characteristics of the flow, we examine wavelength and wave angle characteristics of the disturbances as they propagate downstream. The evolution of the disturbance wavelength (λ/δ, where δ is the boundary-layer thickness) is shown in Figs. 8a–8c for disturbances originating at θ = 20, 60, and 100 deg, respectively. For the disturbances originating at 20 deg, the ratio of λ/δ varies from ≈4 to ≈7 as frequency is increased. These ratios are nearly constant in the streamwise direction for a fixed frequency. Crossflow-type instabilities can be associated with the lower ratios, and TS-type disturbances with the higher ratios. The results for disturbances originating at θ = 60 and 100 deg are much different. For these cases, the ratio λ/δ is approximately 4 near the critical point, irrespective of the frequency. As the disturbances propagate downstream, two distinct trends are seen—either the ratio λ/δ begins to increase rapidly or it remains nearly constant. For purposes of discussion, focus on the disturbances originating at θ = 100 deg. Note that, for the disturbance f = 400 Hz, the ratio of λ/δ remains ≈4 as the disturbance propagates downstream. During the evolution of

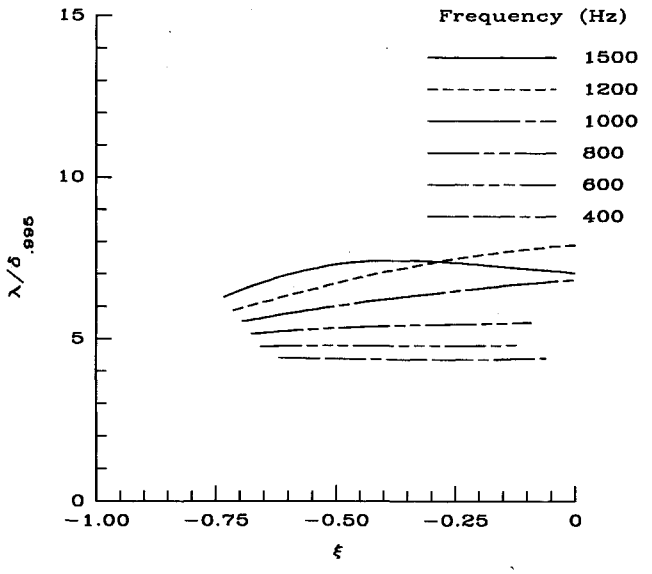

a) θ = 20 deg

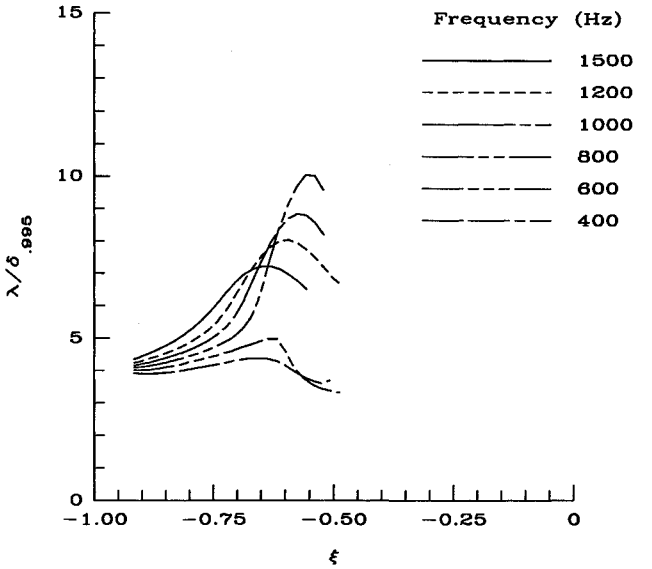

b) θ = 60 deg

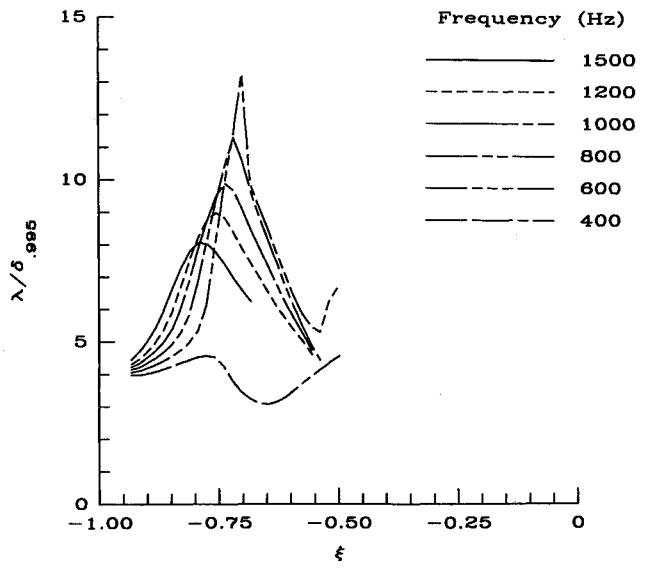

c) θ = 100 deg

Fig. 8 Ratio of disturbance wavelength to boundary-layer thickness as a function of frequency and streamwise location.

the disturbance of frequency f = 600 Hz, this ratio rapidly increases to 13, and then decreases to 5. These increases are also observed for f = 800–1500 Hz, although the maximum ratio of λ/δ becomes progressively smaller and moves somewhat upstream with increasing frequency. These higher values of λ/δ are characteristic of TS-type instabilities. Thus, it appears from the normal mode calculation that, for higher frequencies, the type of disturbance evolves from the crossflow type to TS and back to crossflow. Whether such changes take place physically can only be answered by performing a global analysis involving various modes.

These trends can be further verified by looking at the wave angle of the disturbance as a function of streamwise location, as shown in Figs. 9a–9c. We define the wage angle ψ with respect to the freestream inviscid flow (see Fig. 2). If $\psi = 0$, the wave vector k is aligned in the inviscid flow direction, which is indicative of TS-type disturbances. If $\psi \approx \pm 90$ deg, then the wave vector k is aligned perpendicular to the inviscid flow, and this indicates crossflow-type instabilities. Of course, these classifications are idealized, and in practice some intermediate wave angle may result. Figure 9a shows that, for the lower frequencies, the disturbances originating at θ = 20 deg are primarily of the crossflow type. As the frequencies are increased, $|\psi|$ decreases, and thus, an evolution toward TS-type disturbances has occurred. For the cases in which the disturbances originate at θ = 60 and 100 deg, a rapid change in the wave angle from ≈ -85 to 0 deg is seen for the higher frequencies; for the lowest frequencies, the wave angle remains near −85 deg. Thus, two distinct types of disturbances evolve in the streamwise direction. For the case in which the disturbances originate at θ = 100 deg, the disturbance wave angle of the higher frequencies becomes positive at $\xi \approx -0.75$ and $\theta \approx 130$ deg (corresponding to the approximate location at which the pressure gradient becomes adverse). This indicates a continuing evolution of the disturbance from TS to crossflow type. In other words, we see a continuous shift of the disturbance orientation from negative to positive values of ψ during downstream propagation. Coupled with this shift is an analagous shift in the disturbance wavelength. Thus, the plots of wave angle vs axial location complement/confirm the conclusions arrived at through the previous examination of the disturbance wavelengths.

We now investigate this change in orientation of the crossflow instability in greater detail. For purposes of discussion, we focus on the disturbance frequency f = 600 Hz originating at θ = 100 deg. Recall that there is a rapid change in the wave angle ψ from relatively large negative to large positive values over a short distance (see Fig. 9c). We consider five points along the trajectory curve determined by this disturbance (see Fig. 6). Point 1 is near the critical point, point 2 is farther down the trajectory, point 3 is just upstream of the location of rapid change in wave angle, point 4 is slightly downstream of this location, and finally, point 5 is far downstream (near the location at which N = 10). The exact locations are indicated in the figures to follow. In the following paragraphs we discuss the properties of the mean flow at these five points.

The crossflow velocity profiles are plotted as a function of ζ (the wall-normal boundary-layer coordinate) in Fig. 10. The crossflow velocity is everywhere positive at point 1. At point 2, the magnitude of the crossflow velocity has diminished considerably, although it is still positive. At point 3, the ζ derivative of the crossflow velocity at the wall is nearly zero. Although it is difficult to discern from the figure, at point 4, a small region of reverse crossflow appears near the wall. Thus, we identify the rapid change in the wave angle ψ (and from negative to positive) with the location at which $\partial U_n/\partial\zeta = 0$ at the wall (where U_n is in the direction normal to the inviscid flow velocity vector). In other words, the wave-front orientation is determined by the sign of the crossflow velocity near the wall, and this may be opposite to the primary direction of the crossflow. We have verified this conclusion at several other locations on the ellipsoid where $\partial U_n/\partial\zeta = 0$ at the wall. Far-

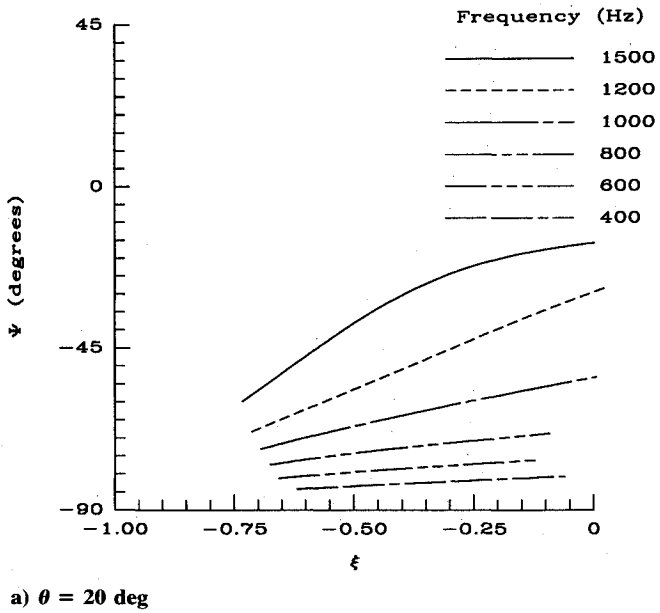

a) θ = 20 deg

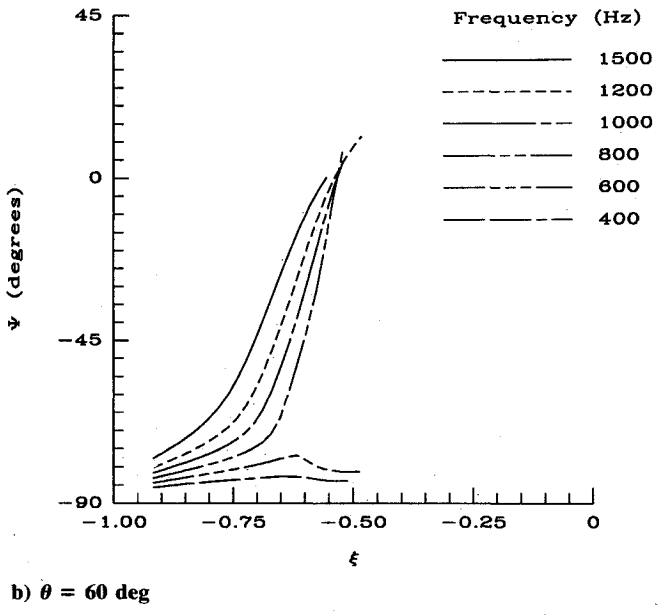

b) θ = 60 deg

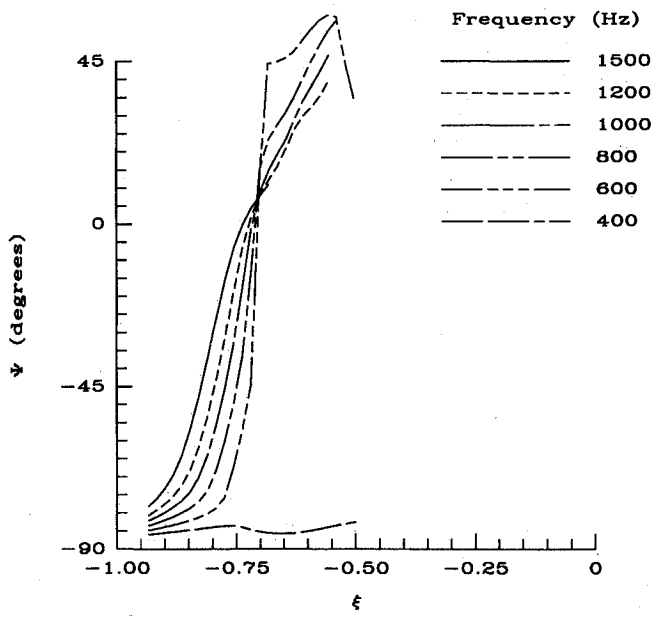

c) θ = 100 deg

Fig. 9 Disturbance wave angle as a function of frequency and streamwise location.

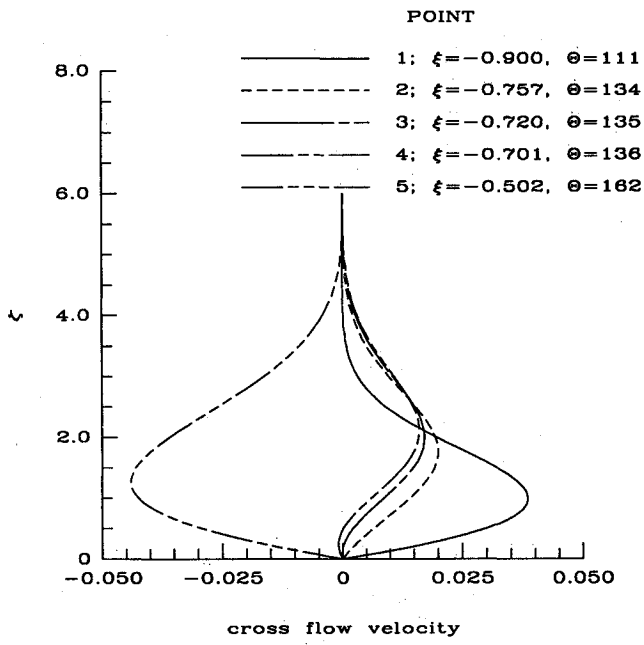

Fig. 10 Crossflow velocity profiles at selected locations along the integration path for a disturbance of 600 Hz originating at θ = 100 deg near the critical point.

ther downstream, at point 5, the reversal of the crossflow velocity (which is caused by a change in the sign of the pressure gradient) is complete and, thus, the instability is again primarily of the crossflow type, although oriented in the opposite direction. In addition, we can expect that the stability calculations become very sensitive as $\partial U_n/\partial\zeta$ approaches zero at the wall. The reason for this sensitivity will become apparent in the following paragraphs.

To understand better the stability characteristics of the profiles at these points, we plot, in Fig. 11, growth rate vs wave angle for the constant frequency of 600 Hz. Recall that point 1 is slightly downstream of the critical point. At this location, the unstable wave angle range is between -77 and -87 deg, with a maximum growth rate of 0.24×10^{-2}. In addition, no unstable regions exist for positive ψ. At point 2, we see that the range of unstable wave angles has increased to include positive values of ψ. However, the most unstable angles are still oriented in the direction of negative ψ. At point 3 (just upstream of the rapid wave angle change), two local maxima exist oriented at $\psi \approx -45$ and 45 deg. In addition, the unstable region has expanded to -85 deg $\leq \psi \leq$ 85 deg, and this distribution is quite symmetric about $\psi = 0$. At point 4, the most unstable disturbance is oriented at ψ = 45 deg. Note that this rapid change has taken place over a very short distance. So, again we see that the change in the crossflow velocity profile near the wall plays an important role in the stability characteristics of the flow. At point 5, the most unstable disturbances are located at $\psi \approx 35$ deg, and there are no other local maxima in the distribution. The instabilities are oriented predominantly in the positive ψ direction. The stability calculations are very sensitive in the regions defined by points 3 and 4, and care must be taken to ensure convergence to the most unstable eigenvalue.

In Fig. 12, we plot $(\alpha u + \beta v - \omega_r)$ (for the most amplified wave angles) vs η, from which we can determine the location of the critical layer (where $\alpha u + \beta v = \omega_r$). Here, η represents the nondimensional coordinate z^*/δ^*, where δ^* is the displacement thickness in the x direction and z^* is the dimensional distance normal to the surface. For points 1 and 2, the critical layer occurs at $\eta \approx 1.5$, whereas for points 3–5, the critical layer occurs at $\eta \approx 0.5$. This indicates that the critical layer rapidly moves lower within the boundary layer as the pressure gradient becomes adverse. The location of the in-

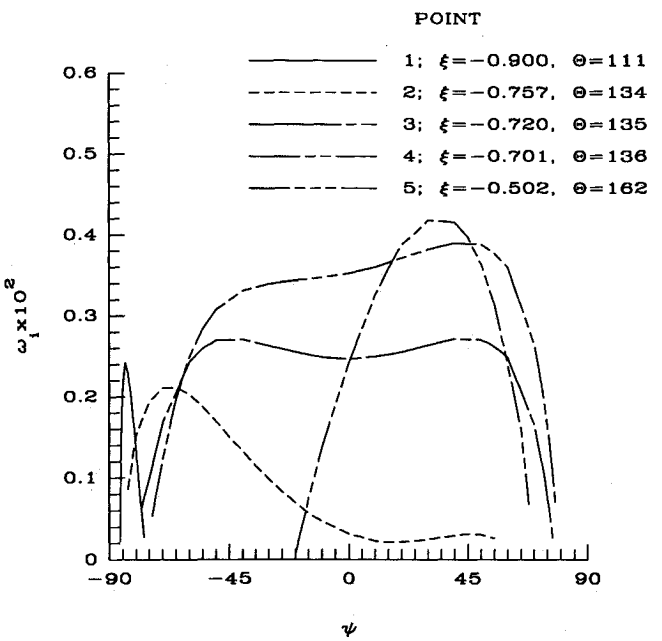

Fig. 11 Growth rate vs wave angle at selected locations along the integration path for a disturbance of 600 Hz originating at θ = 100 deg near the critical path.

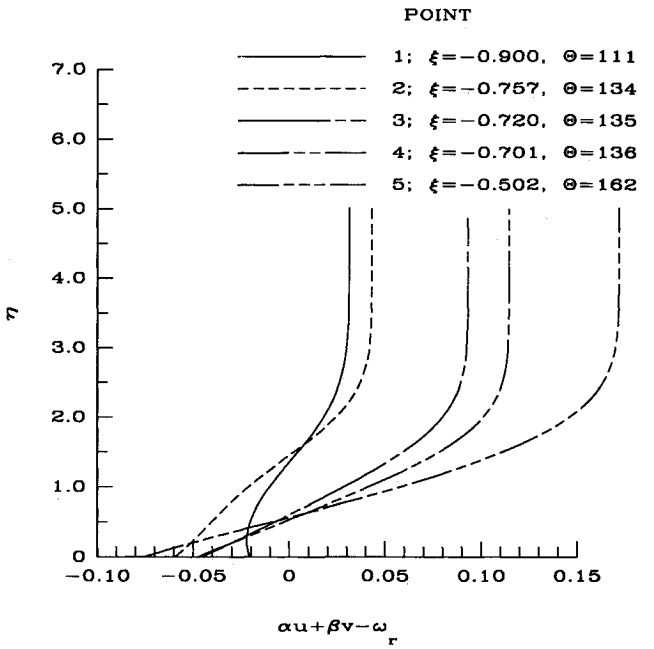

Fig. 13 Second derivative of meanflow velocity component in the direction of the wave-number vector at selected locations along the integration path.

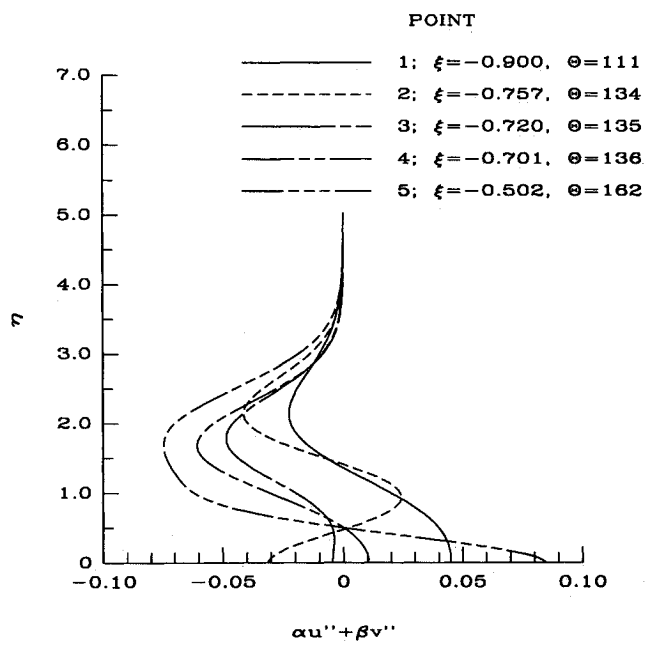

Fig. 12 Effective meanflow velocity profiles in the wave coordinates at selected locations along the integration path.

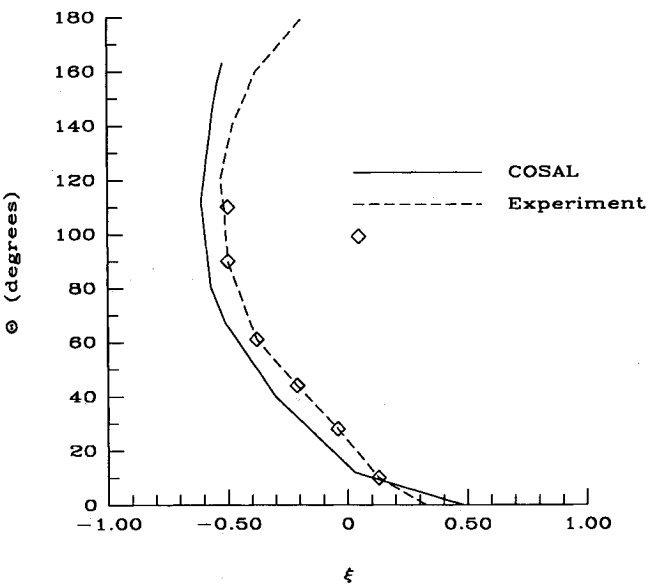

Fig. 14 Comparison of theoretical and experimentally determined[5] locations for the onset of transition: theoretical calculations based on N = 10.

flection points is shown in Fig. 13 by the line $\alpha u'' + \beta v'' = 0$. The inflection point for point 1 is at $\eta \approx 1.4$. For point 2, inflection points exist at $\eta \approx 1.4$ and ≈ 0.5. For points 4 and 5, a single inflection point occurs at $\eta \approx 0.5$. Note that no inflection point is present in the profile at point 3. Thus, the inflection points that are present lie near the critical layers (with the exception of the lower inflection point at 2) and indicate inflectional instabilities. The instability (for $\psi \approx -45$ deg) at point 3 would be viscous in nature.

With an understanding of the basic instability mechanisms that are important for the case of an ellipsoid at incidence, we now turn to the task of predicting the transition front. The transition front obtained using COSAL is compared with the experimental results of Meier and Kreplin[5] in Fig. 14. The theoretical transition front is also shown as a short-dashed line in Fig. 4, the contour plot of constant crossflow Reynolds number. Transition was assumed to occur for N = 10. The overall agreement between experiment and theory is good. Near the windward edge (θ = 0 deg), where two-dimensional TS-type disturbances are responsible for transition, the predicted location of transition is about 10% downstream of the experimental results. For the flowfield at $\theta \geq 20$ deg, for which the instabilities are predominately of the crossflow type, the predicted transition front occurs approximately 10% upstream of the experimental results. The degree of agreement is similar to that obtained by Cebeci and Chen,[3] who used the spatial formulation of the stability problem. The present results might be improved if the displacement thickness were taken into account when calculating the inviscid solution.

IV. Conclusions

This paper considered the linear stability of the three-dimensional boundary layer formed over a prolate spheroid at an angle of attack of 10 deg. The location of the onset of transition, computed using the e^N method, with a value of $N = 10$, agrees quite well with the location determined experimentally by Meier and Kreplin.[5] The differences are greatest near the leeward portion of the spheroid. These differences may be due to effects such as wave-front curvature. Improvement may also be gained by employing an interactive boundary-layer technique in the computation of the mean flow. At any rate, the purpose of the N-factor calculations is to provide a rapid, inexpensive means of transition prediction, and to this extent, the calculations were successful.

A detailed study of the disturbance characteristics reveals that, based on group velocity considerations, TS-type disturbances tend to follow paths of constant θ, whereas crossflow-type disturbances tend to propagate around the spheroid. This indicates that, to be consistent, amplification rates should be integrated along a path determined by the group velocity ratio rather than the inviscid flow streamlines.

Acknowledgments

This work was funded by the Theoretical Flow Physics Branch, Fluid Mechanics Division, NASA Langley Research Center under Contract NAS1-18240. The first author is thankful to J. E. Harris, V. Iyer, and Y.-S. Wie for several useful discussions on boundary-layer computation.

References

[1]Smith, A. M. O., and Gamberoni, N., "Transition, Pressure Gradient, and Stability Theory," Douglas Aircraft Co., Long Beach, CA, Rept. ES 26388, Aug. 1956.

[2]Malik, M. R., "Stability Theory for Laminar Flow Control Design," *Viscous Drag Reduction in Boundary Layers*, edited by A. Richard Seebass, Vol. 123, Progress in Astronautics and Aeronautics, AIAA, Washington, DC, 1990.

[3]Cebeci, T., and Chen, H. H., "Prediction of Transition on Airfoils with Separation Bubbles, Swept Wings and Bodies of Revolution at Incidence," *Symposium on Numerical and Physical Aspects of Aerodynamic Flows*, Long Beach, CA, Jan. 1989.

[4]Malik, M. R., "COSAL—A Black Box Compressible Stability Analysis Code for Transition Prediction in Three-Dimensional Boundary Layers," NASA CR-165925, May 1982.

[5]Meier, H. U., and Kreplin, H., "Experimental Investigation of the Boundary Layer Transition and Separation on a Body of Revolution," *Zeitschrift Für Flugwissenschaften und Weltraum-forschung*, Vol. 4, No. 2, 1980, pp. 65–71.

[6]Wie, Y.-S., "A Three-Dimensional, Compressible, Laminar Boundary-Layer Method for General Fuselages," NASA CR-4292, Vol. I, May 1990.

[7]Matsuno, K., "A Vector-Oriented Finite Difference Scheme for Calculating Three-dimensional Compressible Laminar and Turbulent Boundary Layers on Practical Wing Configurations," AIAA Paper 81-1020, June 1981.

[8]Cebeci, T., Khattab, K. H., and Stewartson, K., "Three-Dimensional Laminar Boundary Layers and the OK of Accessibility," *Journal of Fluid Mechanics*, Vol. 107, 1981, pp. 57–87.

[9]Faulkner, S. M., Hess, J. L., Smith, A. M. O., and Liebeck, R. H. "Charts and Formulas for Estimating Velocity Fields in Incompressible Flow," Douglas Aircraft Co., Rept. LB 32707, Long Beach, CA, 1968.

[10]Malik, M. R., and Orszag, S. A., "Efficient Computation of the Stability of Three-Dimensional Compressible Boundary Layers," AIAA Paper 81-1277, 1981.

[11]Gaster, M., "A Note on the Relation Between Temporally Increasing and Spatially Increasing Disturbances in Hydrodynamic Stability," *Journal of Fluid Mechanics*, Vol. 14, 1962, pp. 222–224.

[12]Balakumar, P., and Malik, M. R., "Waves Produced From a Harmonic Point Source in a Supersonic Boundary Layer," AIAA Paper 91-1646, 1991.

[13]Mack, L. M. "On the Stability of the Boundary Layer on a Transonic Swept Wing," AIAA Paper 79-0264, Jan. 1979.

[14]Malik, M. R., and Poll, D. I., "Effect of Curvature on Three-Dimensional Boundary-Layer Stability," *AIAA Journal*, Vol. 23, No. 9, 1985, pp. 1362–1369.